The Astrophysical Journal Letters, 783:L21 (6pp), 2014 March 1 doi:10.1088/2041-8205/783/1/L21

RELATIVISTIC RECONNECTION: AN EFFICIENT SOURCE OF NON-THERMAL PARTICLES

Lorenzo Sironi[1,3] and Anatoly Spitkovsky[2]
[1] Harvard-Smithsonian Center for Astrophysics, 60 Garden Street, Cambridge, MA 02138, USA; lsironi@cfa.harvard.edu
[2] Department of Astrophysical Sciences, Princeton University, Princeton, NJ 08544-1001, USA; anatoly@astro.princeton.edu
Received 2013 December 23; accepted 2014 January 21; published 2014 February 18

ABSTRACT

In magnetized astrophysical outflows, the dissipation of field energy into particle energy via magnetic reconnection is often invoked to explain the observed non-thermal signatures. By means of two- and three-dimensional particle-in-cell simulations, we investigate anti-parallel reconnection in magnetically dominated electron–positron plasmas. Our simulations extend to unprecedentedly long temporal and spatial scales, so we can capture the asymptotic state of the system beyond the initial transients, and without any artificial limitation by the boundary conditions. At late times, the reconnection layer is organized into a chain of large magnetic islands connected by thin X-lines. The plasmoid instability further fragments each X-line into a series of smaller islands, separated by X-points. At the X-points, the particles become unmagnetized and they get accelerated along the reconnection electric field. We provide definitive evidence that the late-time particle spectrum integrated over the whole reconnection region is a power law whose slope is harder than -2 for magnetizations $\sigma \gtrsim 10$. Efficient particle acceleration to non-thermal energies is a generic by-product of the long-term evolution of relativistic reconnection in both two and three dimensions. In three dimensions, the drift-kink mode corrugates the reconnection layer at early times, but the long-term evolution is controlled by the plasmoid instability which facilitates efficient particle acceleration, analogous to the two-dimensional physics. Our findings have important implications for the generation of hard photon spectra in pulsar winds and relativistic astrophysical jets.

Key words: acceleration of particles – galaxies: jets – gamma-ray burst: general – magnetic reconnection – pulsars: general – radiation mechanisms: non-thermal

Online-only material: animations, color figures

1. INTRODUCTION

It is generally thought that pulsar winds and the relativistic jets of blazars and gamma-ray bursts (GRBs) are launched hydromagnetically (Spruit 2010). Since the energy is initially carried in the form of Poynting flux, how the field energy is transferred to the plasma to power the observed emission is a fundamental question. Field dissipation via magnetic reconnection is often invoked as a source of the accelerated particles required to explain the non-thermal signatures of pulsar wind nebulae (PWNe; Lyubarsky & Kirk 2001; Lyubarsky 2003; Kirk & Skjæraasen 2003; Pétri & Lyubarsky 2007), jets from active galactic nuclei (Romanova & Lovelace 1992; Giannios et al. 2009; Giannios 2013), and GRBs (Thompson 1994, 2006; Spruit et al. 2001; Lyutikov & Blandford 2003; Giannios 2008). Despite decades of research, the efficiency of magnetic reconnection in generating non-thermal particles is not well understood (Hoshino & Lyubarsky 2012).

In astrophysical jets, reconnection proceeds in the "relativistic" regime, since the magnetic energy per particle can exceed the rest mass energy. While the steady-state dynamics of relativistic reconnection has been well characterized by analytical studies (Lyutikov & Uzdensky 2003; Lyubarsky 2005), the process of particle acceleration can only be captured from first principles by means of fully kinetic particle-in-cell (PIC) simulations. Energization of particles in relativistic reconnection has been investigated in a number of PIC studies, both in two dimensions (2D; Zenitani & Hoshino 2001, 2007; Jaroschek et al. 2004; Bessho & Bhattacharjee 2005, 2007, 2012; Daughton & Karimabadi 2007; Lyubarsky & Liverts 2008) and three dimensions (3D; Zenitani & Hoshino 2008; Yin et al. 2008; Liu et al. 2011; Sironi & Spitkovsky 2011a, 2012; Kagan et al. 2013; Cerutti et al. 2014). However, no consensus exists as to whether relativistic reconnection results self-consistently in non-thermal particle acceleration (Sironi & Spitkovsky 2011a), rather than just heating (Cerutti et al. 2012).

In this work, we employ 2D and 3D PIC simulations to follow the evolution of relativistic reconnection in pair plasmas to unprecedentedly long time and length scales, focusing on particle acceleration. We consider the case of anti-parallel fields, without a guide field aligned with the electric current in the sheet. It has been argued that this configuration produces non-thermal particles only in 2D, whereas in 3D the drift-kink (DK) mode would broaden the current sheet, inhibiting particle acceleration (Zenitani & Hoshino 2008; Cerutti et al. 2014). By performing large-scale simulations evolved to long times, we conclusively show that acceleration of particles to non-thermal energies is a *generic* by-product of relativistic reconnection in pair plasmas, in both 2D and 3D. The accelerated particles populate a power-law distribution, whose spectral slope is harder than -2 for magnetizations $\sigma \gtrsim 10$. Relativistic magnetic reconnection is then a viable source of non-thermal emission from magnetically dominated astrophysical flows.

2. STRUCTURE OF THE RECONNECTION LAYER

We use the 3D electromagnetic PIC code TRISTAN-MP (Buneman 1993; Spitkovsky 2005) to study relativistic reconnection in 2D and 3D. The reconnection layer is set up in Harris equilibrium, with the magnetic field $\boldsymbol{B} = -B_0\,\hat{\boldsymbol{x}}\tanh(2\pi y/\Delta)$ reversing at $y = 0$. The field strength is parameterized by the magnetization $\sigma = B_0^2/4\pi mnc^2 = (\omega_c/\omega_{\rm p})^2$, where $\omega_c = eB_0/mc$ is the Larmor frequency and $\omega_{\rm p} = \sqrt{4\pi ne^2/m}$ is the plasma frequency for the electron–positron plasma outside

[3] NASA Einstein Postdoctoral Fellow.

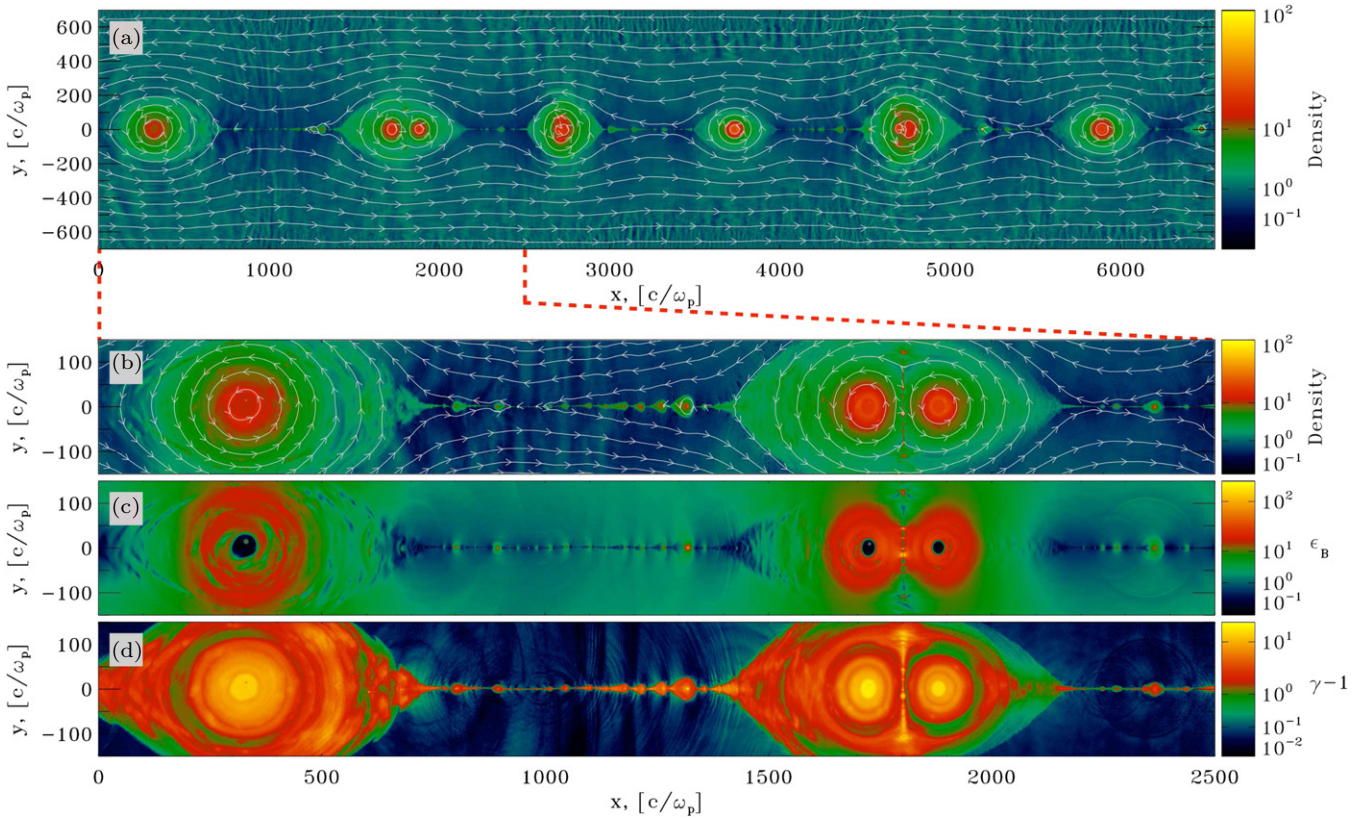

Figure 1. Structure of the reconnection layer at $\omega_p t = 3000$ (so, $\omega_c t \sim 10^4$), from a 2D simulation of $\sigma = 10$ reconnection. The box extends along x over $\sim 6550\, c/\omega_p$ (65,536 cells), and along y over $\sim 6000\, c/\omega_p$ ($\sim$60,000 cells), but along y it will expand even more at later times (we only show a subset of the domain along y). We present (a), (b) particle density, in units of the density far from the sheet (with overplotted magnetic field lines), (c) magnetic energy fraction $\epsilon_B = B^2/8\pi mnc^2$, and (d) mean kinetic energy per particle.

(A color version and animations of this figure are available in the online journal.)

the layer. We focus on the regime $\sigma \geqslant 1$ of relativistic reconnection. The magnetic pressure outside the current sheet is balanced by the particle pressure in the sheet by adding a component of hot plasma with overdensity η relative to the cold particles outside the layer (having $k_B T/mc^2 = 10^{-4}$). From pressure equilibrium, the temperature inside the sheet is $k_B T_h/mc^2 = \sigma/2\eta$. We typically employ $\eta = 3$ and $\Delta = 20\, c/\omega_p$ (c/ω_p is the plasma skin depth), but we have tested that our results at late times do not depend on the initialization of the current sheet (L. Sironi 2014, in preparation; hereafter S14).

In 2D, the computational domain is periodic in the x-direction (in 3D, in x and z), but we have extensively tested that the results reported in this work are not artificially affected by our periodic boundaries (which is often an issue for smaller simulations, S14). Along the y-direction, we employ two moving injectors (receding from $y = 0$ at the speed of light along $\pm\hat{y}$) and an expanding simulation box (S14). The two injectors constantly introduce fresh magnetized plasma into the simulation domain. This permits us to evolve the system as far as the computational resources allow, retaining all the regions that are in causal contact with the initial setup. Such choice has clear advantages over the fully periodic setup that is commonly employed, where the limited amount of particles and magnetic energy will necessarily inhibit the evolution of the system to long times.

For our reference case $\sigma = 10$, we resolve the plasma skin depth with $c/\omega_p = 10$ cells in 2D and 5 cells in 3D, and for higher magnetizations we scale up the resolution by $\sqrt{\sigma/10}$, so that the Larmor gyration period $2\pi/\omega_c = 2\pi/\sqrt{\sigma}\,\omega_p$ is resolved with at least a few time steps. We typically employ four particles per cell in 2D and one per cell in 3D (on average, including both species), but we have extensively tested that the physics at late times is the same when using up to 64 (in 2D) or 8 (in 3D) particles per cell (S14).

Magnetic reconnection starts from numerical noise (unlike most other studies, we do not artificially perturb the magnetic flux function to trigger reconnection). As a result of the tearing instability, the reconnection layer breaks into a series of magnetic islands, separated by X-points. Over time, the islands coalesce and grow to larger scales (see Daughton & Karimabadi 2007 for similar conclusions in non-relativistic reconnection). The structure of the reconnection region at late times is presented in Figure 1 from our large-scale 2D simulation in a $\sigma = 10$ pair plasma. The reconnection layer at $\omega_p t = 3000$ is divided into six major islands, separated by thin X-lines (Figure 1(a)). By zooming into the region $x \lesssim 2500\, c/\omega_p$, as indicated by the dashed red lines below Figure 1(a), we show that each X-line is further fragmented into a chain of smaller islands, as a result of the secondary tearing mode (or "plasmoid instability") discussed by Uzdensky et al. (2010). The secondary islands appear as overdense regions at $700\, c/\omega_p \lesssim x \lesssim 1400\, c/\omega_p$ in Figure 1(b), which are filled with hot particles (Figure 1(d)) confined by strong fields (Figure 1(c)). In between each pair of secondary islands, a secondary X-point governs the transfer of energy from the fields to the particles. As shown in Section 3,

efficient particle acceleration occurs at the X-points (both at secondary X-points and at the primary X-point located at $x \sim 1000\,c/\omega_{\rm p}$ in Figures 1(b)–(d)).

The cold upstream plasma flows into the X-line at the speed $v_{\rm rec} \simeq 0.08\,c$ (the so-called "reconnection rate"), which is nearly constant over time. As shown in S14, the reconnection rate increases from $v_{\rm rec} \simeq 0.03\,c$ for $\sigma = 1$ to $v_{\rm rec} \simeq 0.12\,c$ for $\sigma = 30$, and it is nearly independent of σ for larger magnetizations (we have tried up to $\sigma = 100$), in agreement with Lyubarsky (2005). After entering the current sheet, the flow is advected toward the major islands by the reconnected magnetic field (in the inset of Figures 1(b)–(d), the major islands lie at $200\,c/\omega_{\rm p} \lesssim x \lesssim 500\,c/\omega_{\rm p}$ and $1600\,c/\omega_{\rm p} \lesssim x \lesssim 1900\,c/\omega_{\rm p}$). The fast reconnection exhausts move with a bulk Lorentz factor $\sim\sqrt{\sigma} \simeq 3$, as predicted by Lyubarsky (2005). Eventually, all the particles heated and accelerated by reconnection are trapped within the major islands, which act as reservoirs of particles (Figure 1(b)) and particle energy (Figure 1(d)). There, the magnetic field is also stronger (by effect of compression; Figure 1(c)), so we expect the major islands to dominate the synchrotron emissivity.

Pushed by the ram pressure of the reconnection exhausts, the major islands move along the layer and merge with neighboring islands. Two major islands are coalescing at $x \sim 1800\,c/\omega_{\rm p}$ in Figure 1. The current sheet formed between the two merging islands is tearing unstable, and it breaks into a chain of secondary islands along the y-direction. As shown in S14, the anti-reconnection electric field at the X-points between two merging islands plays an important role in boosting the high-energy particles trapped in the islands to even higher energies.[4]

The evolution of 3D reconnection at late times parallels closely the 2D physics described above, *even in the absence of a guide field*. As shown in Figure 2(a), we find that the early phases are governed by the DK mode, in agreement with previous studies (Zenitani & Hoshino 2008; Cerutti et al. 2014). The DK instability corrugates the current sheet in the z-direction, broadening the layer and inhibiting the early growth of the tearing mode. However, at later times the evolution is controlled by the tearing instability, which produces in the xy plane a sequence of magnetic islands (or rather, tubes) that grow and coalesce over time, analogous to the 2D physics. The reconnection layer at late times is organized into a few major islands (see the overdense plasmoids in Figure 2(b)), separated by underdense regions (transparent in Figure 2(b)) where field dissipation by reconnection is most efficient. In such neutral planes, the secondary tearing instability can operate, producing a chain of smaller magnetic tubes (see the region at $500\,c/\omega_{\rm p} \lesssim x \lesssim 700\,c/\omega_{\rm p}$ near the 2D slice at $z = 130\,c/\omega_{\rm p}$ in Figure 2(b)), reminiscent of the secondary islands observed in 2D. In short, at late times the 3D physics closely parallels the 2D evolution presented above (albeit with a reduced reconnection rate, $v_{\rm rec} \simeq 0.02\,c$ in 3D versus $v_{\rm rec} \simeq 0.08\,c$ in 2D). As shown in Section 3, this has important implications for the acceleration performance of relativistic reconnection in 3D. Earlier simulations, being limited to early times and/or small boxes, could not capture the long-term evolution of 3D reconnection, with the emergence of the dominant tearing mode beyond the DK phase.

[4] The hierarchical process of island formation and merging proceeds as long as the evolution is not artificially inhibited by the boundary conditions. This emphasizes the importance of large-scale simulations to properly capture the late-time physics.

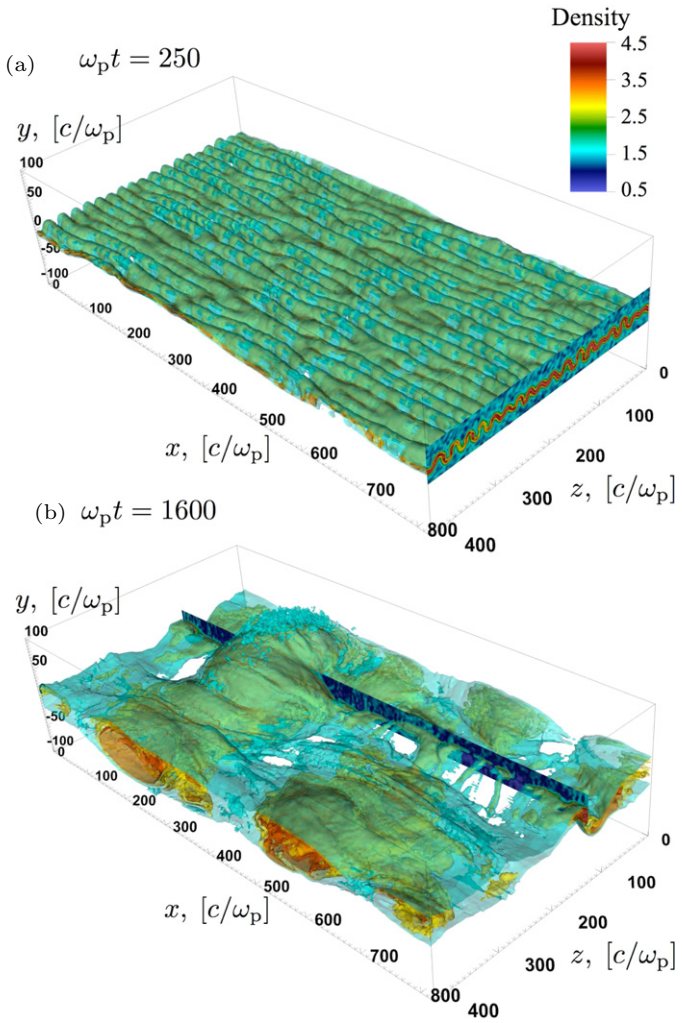

Figure 2. Structure of particle density at (a) $\omega_{\rm p}t = 250$ and (b) $\omega_{\rm p}t = 1600$, from a 3D simulation of $\sigma = 10$ reconnection without guide field. The simulation box extends over $\sim 820\,c/\omega_{\rm p}$ (4096 cells) along x, $\sim 410\,c/\omega_{\rm p}$ (2048 cells) along z, and it expands at the speed of light along $\pm\hat{\mathbf{y}}$ (we only show a subset of the domain along y). The 2D slices in the top and bottom panels (at $x = 820\,c/\omega_{\rm p}$ and $z = 130\,c/\omega_{\rm p}$, respectively) show the particle density.

(A color version and animation of this figure are available in the online journal.)

3. SPECTRUM AND ACCELERATION MECHANISM

In Figure 3 we present the time evolution of the particle energy spectrum integrated over the whole reconnection region (more precisely, for $|y| \lesssim 500\,c/\omega_{\rm p}$), from a 2D simulation with $\sigma = 10$.[5] At the X-lines, more than half of the initial magnetic energy is converted into particle kinetic energy. Figure 3 shows that a self-consistent by-product of relativistic reconnection is the generation of a broad non-thermal spectrum extending to ultra-relativistic energies. For $\sigma = 10$, the spectrum at $\gamma \gtrsim 1.5$ can be fitted with a power law of slope $p \equiv -d\log N/d\log\gamma \sim 2$ (dotted red line).[6] The spectrum clearly departs from a Maxwellian with mean energy $(\sigma + 1)\,mc^2$ (red dashed line, assuming complete field dissipation). As shown in the inset of

[5] In our spectra, we do not include the hot particles that were initialized in the sheet to provide pressure support against the external magnetic field. With this choice, the late-time spectrum is nearly independent from the current sheet initialization (S14).

[6] The peak at $\gamma \lesssim 1.5$ contains the cold particles that are drifting toward the sheet at the reconnection speed $v_{\rm rec} \simeq 0.08\,c$.

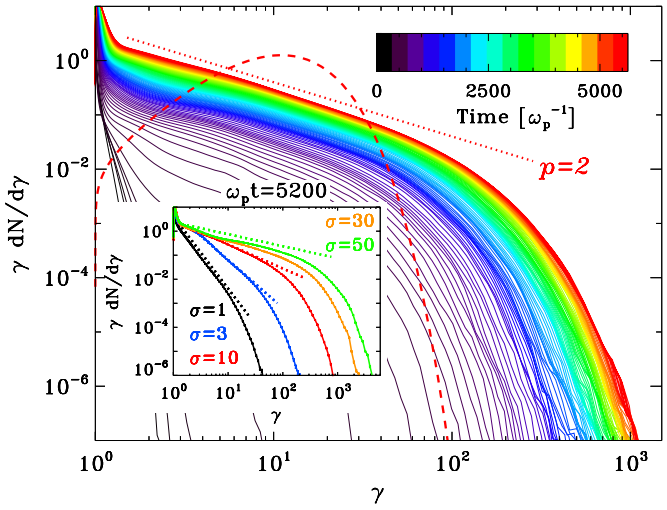

Figure 3. Temporal evolution of particle energy spectrum, from a 2D simulation of $\sigma = 10$ reconnection. The spectrum at late times resembles a power law with slope $p = 2$ (dotted red line), and it clearly departs from a Maxwellian with mean energy $(\sigma + 1)\,mc^2$ (dashed red line, assuming complete field dissipation). The dependence of the spectrum on the magnetization is shown in the inset, as indicated in the legend. The dotted lines refer to power-law slopes of -4, -3, -2, and -1.5 (from black to green).

(A color version of this figure is available in the online journal.)

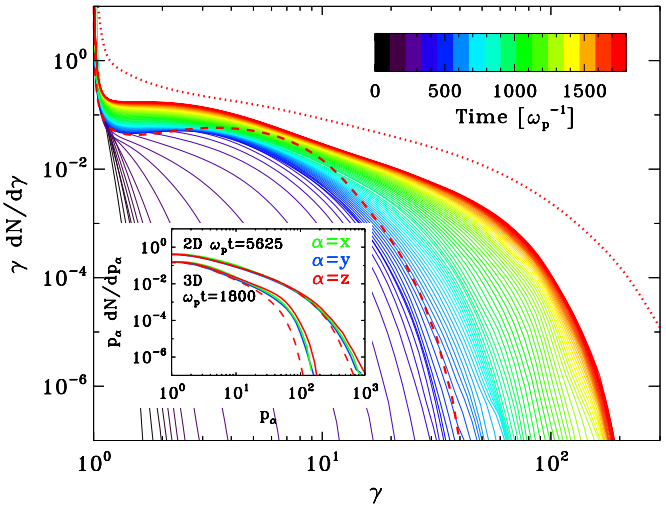

Figure 4. Temporal evolution of particle energy spectrum, from a 3D simulation of $\sigma = 10$ reconnection. The spectra from two 2D simulations with in-plane (out-of-plane) anti-parallel fields are shown with red dotted (dashed) lines. Positron momentum spectrum along x (green), y (blue), $+z$ (red solid), and $-z$ (red dashed), for 2D and 3D is shown in the inset.

(A color version of this figure is available in the online journal.)

Figure 3, the power-law slope depends on the magnetization, and it is harder for higher σ ($p \sim 1.5$ for $\sigma = 50$, compare the solid and dotted green lines). The slope is steeper for lower magnetizations ($p \sim 4$ for $\sigma = 1$, solid and dotted black lines), approaching the result from earlier studies of non-relativistic reconnection, which found poor acceleration efficiencies (Drake et al. 2010).

As described below, the power-law shape of the energy spectrum is established as the particles interact with the X-points, where they get accelerated by the reconnection electric field. After being advected into the major islands shown in Figure 1(a), the particles experience a variety of other acceleration processes (Drake et al. 2006; Oka et al. 2010), but the power-law index does not appreciably change. As described in S14, the anti-reconnection electric field between two merging islands plays a major role for the increase in the spectral cutoff shown in Figure 3. For magnetizations $\sigma \gtrsim 10$ that yield $p \lesssim 2$, the increase in maximum energy is expected to terminate, since the mean energy per particle cannot exceed $(\sigma + 1)\,mc^2$.[7] For a power law of index $1 < p < 2$ starting from $\gamma_{\rm min} = 1$, the maximum Lorentz factor should saturate at $\gamma_{\rm max} \sim [(\sigma + 1)\,(2 - p)/(p - 1)]^{1/(2-p)}$.

So far, we have shown that 2D simulations of relativistic reconnection produce hard populations of non-thermal particles. The validity of our conclusions may be questioned if the structure of X-points in 3D is significantly different from 2D. In particular, the DK mode is expected to result in heating, not in particle acceleration (Zenitani & Hoshino 2007). In Figure 4 we follow the temporal evolution of the particle spectrum in a 3D simulation with $\sigma = 10$. We confirm the conclusions of earlier studies (Zenitani & Hoshino 2008; Cerutti et al. 2014) that the spectrum at early times is quasi-thermal (black to blue lines in Figure 4), and it resembles the distribution resulting from the DK mode (the red dashed line shows the spectrum from a 2D simulation with out-of-plane anti-parallel fields, to isolate the contribution of the DK mode). As shown in Section 2, the DK mode grows the fastest, but the sheet evolution at late times is controlled by the tearing instability, analogous to 2D simulations with in-plane fields. The X-points formed by the tearing mode can efficiently accelerate non-thermal particles, and the spectrum at late times (cyan to red lines in Figure 4) presents a pronounced high-energy power law. The power-law slope is $p \sim 2.3$, close to the $p \sim 2$ index of 2D simulations with in-plane fields. With respect to the 2D spectrum (dotted red line in Figure 4), the normalization and the upper energy cutoff of the 3D spectrum are smaller, due to the lower reconnection rate ($v_{\rm rec} \simeq 0.02\,c$ in 3D versus $v_{\rm rec} \simeq 0.08\,c$ in 2D), so that fewer particles enter the current sheet per unit time, where they get accelerated by a weaker electric field $E_{\rm rec} \sim (v_{\rm rec}/c)\,B_0$. Analogous to 2D, we argue that the anti-reconnection electric field in between merging plasmoids drives the increase in the high-energy spectral cutoff shown in Figure 4.

The mechanism of particle acceleration at X-points is presented in Figure 5 in the case of a 2D simulation with $\sigma = 10$. We follow the energy evolution of a sample of simulation particles that interact with the sheet in the vicinity of the central X-point (located at $x \sim 135\,c/\omega_{\rm p}$). There, the magnetic energy is smaller than the electric energy (blue region in Figure 5(b)), so the particles become unmagnetized and they get accelerated along z by the reconnection electric field. The final energy of the particles—the color in Figure 5(a) indicates the Lorentz factor measured at the outflow boundary of the X-line—directly correlates with the location at the moment of interaction with the sheet (Larrabee et al. 2003; Bessho & Bhattacharjee 2012). Particles interacting closer to the center of the X-point (darkest blue in Figure 5(b)) are less prone to be advected away along x by the reconnected magnetic field, so they can stay longer in the acceleration region and reach higher Lorentz factors (orange and red lines in Figure 5(a)). A broad distribution is then established as a result of the different energy histories of particles interacting at different distances from the X-point. The particle spectrum at the edge of the acceleration region (the blue area in Figure 5(b)) resembles the form $dN/d\gamma \propto \gamma^{-1/4} \exp[-(4\gamma/\sigma\beta_{\rm rec}^2\lambda)^{1/2}]$

[7] For $\sigma \lesssim 10$ (so, $p \gtrsim 2$), the increase in maximum energy does not stop, but it slows down at late times. As the islands grow bigger they become slower, so the anti-reconnection electric field during mergers gets weaker.

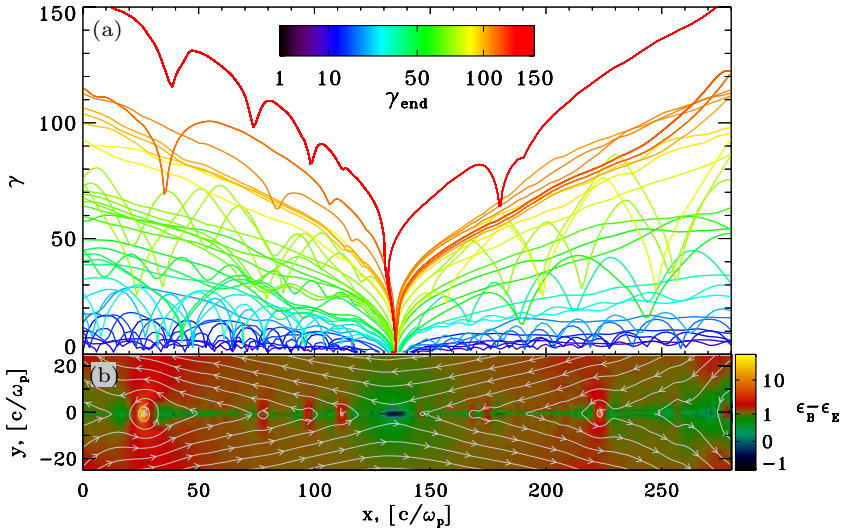

Figure 5. (a) Energy evolution of a sample of selected particles interacting with a major X-point, as a function of the location x along the current sheet. Colors are scaled with $\gamma_{\rm end}$, the Lorentz factor attained at the outflow boundary of the X-line (at $x = 0$ or $280\,c/\omega_{\rm p}$, depending on the particle). (b) $\epsilon_B - \epsilon_E$ at the time when the particles interact with the X-point (here, $\epsilon_E = E^2/8\pi mnc^2$).

(A color version and animation of this figure are available in the online journal.)

predicted by Bessho & Bhattacharjee (2012), where $\beta_{\rm rec} = v_{\rm rec}/c$ and λ is the length of the acceleration region in units of the Larmor radius of the heated particles (with $\langle\gamma\rangle \sim \sigma$). The spectrum of the particles flowing into the major islands still bears memory of this scaling, but it becomes softer due to the addition of low-energy particles injected at the secondary X-points (weaker than the major X-point in Figure 5) or accreted onto the outflowing secondary islands.

After being accelerated along z, the particles are advected along x by the reconnected magnetic field, and they finally enter the major islands shown in Figure 1(a). In the islands, the accelerated particles gyrate in the strong fields shown in Figure 1(c), isotropizing their angular distribution (which was strongly beamed along z close to the X-points, and along x in the reconnection exhausts; see Cerutti et al. 2013). Since most of the particles at late times are contained in the major islands, it is not surprising that the long-term momentum spectra show little signs of anisotropy (see the inset in Figure 4). Even the residual difference between the momentum spectra along $+z$ and $-z$ (red solid and dashed lines, respectively) diminishes at later times (the 2D momentum spectra at $\omega_{\rm p}t = 1800$ were similar to the 3D results in the inset of Figure 4, showing that the anisotropy decays over time).[8]

4. DISCUSSION

By means of large-scale PIC simulations, we have provided definitive evidence that non-thermal particle acceleration is a *generic* by-product of the long-term evolution of relativistic reconnection, in both 2D and 3D. We have focused on the case of anti-parallel reconnection without a guide field. We find that in 3D the DK mode delays the onset of efficient particle acceleration, but the physics at late times is similar to its 2D counterpart. Earlier studies could not capture the late-time evolution that leads to efficient particle acceleration due to insufficient integration times and/or limited computational domains. The particles accelerated by the reconnection electric field at the X-points form a power law with slope p that varies from $p \sim 4$ for $\sigma = 1$ to $p \lesssim 1.5$ for $\sigma \gtrsim 50$. For $\sigma \gtrsim 10$ the index is $p \lesssim 2$, harder than in relativistic shocks (Sironi & Spitkovsky 2011b; Sironi et al. 2013). So, relativistic reconnection is a viable candidate for producing hard spectra in astrophysical non-thermal sources.

Flat electron spectra below GeV energies are required to fit the broadband emission of hotspots in radio galaxies (Stawarz et al. 2007) and the X-ray spectrum of blazars (Celotti & Ghisellini 2008; Sikora et al. 2009). Also, relativistic reconnection in blazars might explain the recently discovered ultra-fast (∼3–5 minutes) TeV flares (Aharonian et al. 2007; Giannios et al. 2009; Nalewajko et al. 2011). In PWNe, the recently detected GeV flares from the Crab Nebula require hard particle spectra with $p \lesssim 2$ (Buehler et al. 2012), and relativistic reconnection has been invoked to explain the temporal variability of the flares (Cerutti et al. 2013). Our first-principles simulations provide a physically grounded model, based on relativistic reconnection, for the generation of hard particle spectra in astrophysics.

L.S. is supported by Einstein grant PF1-120090, and A.S. by NASA grants NNX12AD01G and NNX13AO80G and Simons Foundation grant 267233. The simulations used PICSciE-OIT HPCC at Princeton University, XSEDE under contract TG-AST120010, and NASA HEC.

[8] The particle angular distribution at late times may be different in the presence of a guide field; see S14.

REFERENCES

Aharonian, F., Akhperjanian, A. G., Bazer-Bachi, A. R., et al. 2007, ApJL, 664, L71
Bessho, N., & Bhattacharjee, A. 2005, PhRvL, 95, 245001
Bessho, N., & Bhattacharjee, A. 2007, PhPl, 14, 056503
Bessho, N., & Bhattacharjee, A. 2012, ApJ, 750, 129
Buehler, R., Scargle, J. D., Blandford, R. D., et al. 2012, ApJ, 749, 26
Buneman, O. 1993, in Computer Space Plasma Physics, ed. H. Matsumoto & Y. Omura (Tokyo: Terra Scientific), 67
Celotti, A., & Ghisellini, G. 2008, MNRAS, 385, 283
Cerutti, B., Uzdensky, D. A., & Begelman, M. C. 2012, ApJ, 746, 148
Cerutti, B., Werner, G. R., Uzdensky, D. A., & Begelman, M. C. 2013, ApJ, 770, 147

Cerutti, B., Werner, G. R., Uzdensky, D. A., & Begelman, M. C. 2014, ApJ, 782, 104
Daughton, W., & Karimabadi, H. 2007, PhPl, 14, 072303
Drake, J. F., Opher, M., Swisdak, M., & Chamoun, J. N. 2010, ApJ, 709, 963
Drake, J. F., Swisdak, M., Che, H., & Shay, M. A. 2006, Natur, 443, 553
Giannios, D. 2008, A&A, 480, 305
Giannios, D. 2013, MNRAS, 431, 355
Giannios, D., Uzdensky, D. A., & Begelman, M. C. 2009, MNRAS, 395, L29
Hoshino, M., & Lyubarsky, Y. 2012, SSRv, 173, 521
Jaroschek, C. H., Lesch, H., & Treumann, R. A. 2004, ApJL, 605, L9
Kagan, D., Milosavljević, M., & Spitkovsky, A. 2013, ApJ, 774, 41
Kirk, J. G., & Skjæraasen, O. 2003, ApJ, 591, 366
Larrabee, D. A., Lovelace, R. V. E., & Romanova, M. M. 2003, ApJ, 586, 72
Liu, W., Li, H., Yin, L., et al. 2011, PhPl, 18, 052105
Lyubarsky, Y., & Kirk, J. G. 2001, ApJ, 547, 437
Lyubarsky, Y., & Liverts, M. 2008, ApJ, 682, 1436
Lyubarsky, Y. E. 2003, MNRAS, 345, 153
Lyubarsky, Y. E. 2005, MNRAS, 358, 113
Lyutikov, M., & Blandford, R. 2003, arXiv:astro-ph/0312347
Lyutikov, M., & Uzdensky, D. 2003, ApJ, 589, 893
Nalewajko, K., Giannios, D., Begelman, M. C., Uzdensky, D. A., & Sikora, M. 2011, MNRAS, 413, 333
Oka, M., Phan, T., Krucker, S., Fujimoto, M., & Shinohara, I. 2010, ApJ, 714, 915
Pétri, J., & Lyubarsky, Y. 2007, A&A, 473, 683
Romanova, M. M., & Lovelace, R. V. E. 1992, A&A, 262, 26
Sikora, M., Stawarz, Ł., Moderski, R., Nalewajko, K., & Madejski, G. M. 2009, ApJ, 704, 38
Sironi, L., & Spitkovsky, A. 2011a, ApJ, 741, 39
Sironi, L., & Spitkovsky, A. 2011b, ApJ, 726, 75
Sironi, L., & Spitkovsky, A. 2012, CS&D, 5, 014014
Sironi, L., Spitkovsky, A., & Arons, J. 2013, ApJ, 771, 54
Spitkovsky, A. 2005, in AIP Conf. Proc. 801, Astrophysical Sources of High Energy Particles and Radiation, ed. T. Bulik, B. Rudak, & G. Madejski (Melville, NY: AIP), 345
Spruit, H. C. 2010, in The Jet Paradigm, ed. T. Belloni (Lecture Notes in Physics, Vol. 794; Berlin: Springer), 233
Spruit, H. C., Daigne, F., & Drenkhahn, G. 2001, A&A, 369, 694
Stawarz, Ł., Cheung, C. C., Harris, D. E., & Ostrowski, M. 2007, ApJ, 662, 213
Thompson, C. 1994, MNRAS, 270, 480
Thompson, C. 2006, ApJ, 651, 333
Uzdensky, D. A., Loureiro, N. F., & Schekochihin, A. A. 2010, PhRvL, 105, 235002
Yin, L., Daughton, W., Karimabadi, H., et al. 2008, PhRvL, 101, 125001
Zenitani, S., & Hoshino, M. 2001, ApJL, 562, L63
Zenitani, S., & Hoshino, M. 2007, ApJ, 670, 702
Zenitani, S., & Hoshino, M. 2008, ApJ, 677, 530